Self-Adaptive $ZnMn_2O_4$/α-MnO_2 nanocomposite as an anode material for High-Performance Lithium-Ion batteries

Chandran, Bharath; Babu, Reshma S.; Gonugunta, P.; Osaimany, Padmaraj; Hendrikx, R.W.A.; Taheri, P.; Mol, J.M.C.; Satyanarayana, N.; Ravi Anusuyadevi, P.; More Authors

DOI
10.1016/j.apsusc.2025.164175

Publication date
2025

Document Version
Final published version

Published in
Applied Surface Science

Citation (APA)
Chandran, B., Babu, R. S., Gonugunta, P., Osaimany, P., Hendrikx, R. W. A., Taheri, P., Mol, J. M. C., Satyanarayana, N., Ravi Anusuyadevi, P., & More Authors (2025). Self-Adaptive ZnMn2O4/α-MnO2 nanocomposite as an anode material for High-Performance Lithium-Ion batteries. *Applied Surface Science*, *712*, Article 164175. https://doi.org/10.1016/j.apsusc.2025.164175

Applied Surface Science 712 (2025) 164175

Contents lists available at ScienceDirect

Applied Surface Science

journal homepage: www.elsevier.com/locate/apsusc

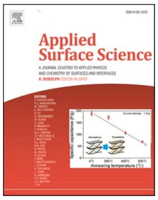

Full Length Article

Self-Adaptive $ZnMn_2O_4$/α-MnO_2 nanocomposite as an anode material for High-Performance Lithium-Ion batteries

Bharath Chandran [a], Reshma S Babu [a], Prasad Gonugunta [b], O. Padmaraj [c], Thamayanthi Panneerselvam [a], R. Murugan [a], Gangineni Ramesh Babu [a], Ruud Hendrikx [b], Peyman Taheri [b], Arjan Mol [b], N. Satyanarayana [a,*], Prasaanth Ravi Anusuyadevi [b,*]

[a] Department of Physics, Pondicherry University, Puducherry 605014, India
[b] Department of Materials Science and Engineering (MSE), Faculty of Mechanical Engineering (ME), Delft University of Technology, Mekelweg 2, 2628 CD Delft, the Netherlands
[c] Department of Physics, Puducherry Technological University, Pondicherry 605014, India

ARTICLE INFO

Keywords:
Lithium-ion batteries
Anode
$ZnMn_2O_4$
α-MnO_2 nanowires
Mixed-type morphology
Microwave-assisted Hydrothermal Method

ABSTRACT

The pursuit of scalable and efficient electrode materials is essential for advancing lithium-ion battery (LIB) technologies. Among the anode candidates, spinel-structured $ZnMn_2O_4$ (ZMO) is attractive due to its high theoretical capacity (~1008 $mAhg^{-1}$), environmental friendliness, and cost-effectiveness. However, large volume expansion during lithium insertion/extraction and poor electrical conductivity limit its long-term performance. Conventional ZMO nanostructure synthesis involves complex, multi-step processes requiring high-temperature calcination, making them time-consuming and unsuitable for large-scale production. To overcome these challenges, we developed a rapid, one-pot microwave-assisted hydrothermal synthesis technique to fabricate a $ZnMn_2O_4$/α-MnO_2 (ZMO/α-MO) nanocomposite. This method reduces processing time and enables in-situ formation of a mixed morphology. The composite consists of nano-polyhedral $ZnMn_2O_4$ integrated with 1D α-MnO_2 nanowires, which buffer volume changes and enhance structural stability during cycling. The synergistic architecture improves electron transport, reduces lithium-ion diffusion paths, and provides superior mechanical resilience. Electrochemical results showed that the ZMO/α-MO nanocomposite as an anode material in the Li half-cell delivered a high discharge capacity of 891.6 $mAhg^{-1}$ at 100 mAg^{-1} after 100 cycles. The electrode exhibited stable cycling across varying current densities and self-adaptive capacity recovery at different rates. These performance enhancements are attributed to improved reaction kinetics enabled by its porous structure, high surface area, and controlled volume expansion of ZMO nanoparticles composited with α-MnO_2 nanowires. This green, scalable, and time-saving synthesis strategy offers promising potential for next-generation high-performance LIBs.

1. Introduction

Over the past decades, the demand for sustainable energy solutions has surged, driving advancements in long-lasting, high-energy–density, energy storage systems with reduced environmental impact. Worldwide, researchers have been motivated to focus on rechargeable lithium-ion batteries (LIBs), which remain the dominant battery technology due to their superior energy density, lightweight design, long cycle life, reliability, and efficiency [1,2]. While alternatives like sodium-ion, solid-state and metal-air batteries are being explored, none have yet surpassed LIBs' overall commercial viability and performance. Therefore, LIBs have been utilized to power everyday portable devices such as smartphones, laptops, digital cameras, etc., and they have also shaped the future of electric vehicle (EV) applications [1,2].

Anodes for LIBs have traditionally been made from graphite, which remains the most successful material. Nevertheless, its limited specific capacity (372 $mAhg^{-1}$) restricts it from developing future batteries with higher capacity and rate capability, which triggered the global interest in identifying alternative anode materials with better electrochemical performance [3–5]. To overcome the aforementioned issues, transition metal oxides (TMOs), such as ferrites, cobaltates, and manganates, have gained attention as alternate anode materials, mainly because of their

---

* Corresponding authors.
E-mail addresses: nallanis2011@gmail.com (N. Satyanarayana), P.RaviAnusuyadevi@tudelft.nl, ranu.prasaanth@gmail.com (P.R. Anusuyadevi).

https://doi.org/10.1016/j.apsusc.2025.164175
Received 31 May 2025; Received in revised form 14 July 2025; Accepted 26 July 2025

higher theoretical capacity, compared to graphite [6,7]. Spinel-structured mixed transition metal oxides (MTMOs), represented by the general formula AB_2O_4 (where A = Zn, Co, Ni, etc. and B = Mn, Fe, Co, etc.), are considered excellent candidates for anode applications. The synergistic effect of two different metals leads to the lower activation energy for electron transfer between cations resulting in better conductivity in MTMOs compared to single metal oxides [8–11].

Among the MTMOs, $ZnMn_2O_4$ (ZMO) is one of the most promising candidates due to its low cost, abundant availability, environmental benignity, and low working potential (~1.3 – 1.5 V) for lithium extraction, compared to cobalt-based oxides [10,12,13]. Besides, $ZnMn_2O_4$ has a high theoretical capacity (~1008 $mAhg^{-1}$), making it an even better alternative anode material for next-generation LIBs [13,14]. Despite this, $ZnMn_2O_4$ still suffers from serious problems like volume expansion during Li^+ ion insertion, resulting in the pulverization of the electrode material and a fading capacity. Moreover, the spinel-structured $ZnMn_2O_4$ shows poor electrical conductivity, which may suppress the reaction kinetics during electrochemical performance [15,16]. These issues are the primary research focus topics for unlocking the potential of $ZnMn_2O_4$ anode material for energy storage applications. Thereby, researchers have developed several nanostructured materials through different approaches, namely porous nanospheres [12,16,17], nanosheets [18–20], nanorods, etc., to mitigate the volume expansion and decrease the diffusion length for Li^+ ions [17–20]. Most conventional synthesis methods for $ZnMn_2O_4$ nanostructures are often complex, time-consuming, and typically require high-temperature treatment of intermediate phases to obtain the porous $ZnMn_2O_4$ nanoparticles. Such approaches are also not favourable for large-scale or energy-efficient anode material production. Moreover, a facile one-pot synthesis of $ZnMn_2O_4$ nanoparticles integrated with a suitable one-dimensional (1D) metal oxide, which can address the inherent volume expansion during cycling, has not been explored yet. In this context, MnO_2 is a promising candidate for forming such a composite with $ZnMn_2O_4$ through a one-pot synthesis. Among its various polymorphs (α, β, γ, δ, and λ types), α-MnO_2 stands out due to its hollandite-type structure with comparatively larger [2 × 2] tunnels formed by corner and edge-shared MnO_6 octahedra. The tunnel framework facilitates rapid lithium-ion diffusion and enhances reaction kinetics [21]. When tailored into 1D nanostructures, α-MnO_2 can exhibit additional advantages such as a high surface-to-volume ratio, improved electron transport pathways, and structural flexibility, all of which help to mitigate volume changes during Li^+ insertion/extraction [22,23]. The 1D α-MnO_2 nanowires can thus serve as a flexible buffer matrix that accommodates the large volume expansion of rigid $ZnMn_2O_4$ nanoparticles, thereby enhancing mechanical stability, reducing structural degradation, and ensuring long-term cycling stability.

Hence, in the present work, an efficient and practical microwave-assisted hydrothermal synthesis technique was developed to produce a mixed-type morphology of $ZnMn_2O_4$/α-MnO_2 (ZMO/α-MO) nanocomposite as an anode material, which could be employed to combine the above-mentioned positive aspects of both $ZnMn_2O_4$ and 1D α-MnO_2 nanostructures. Here, the successful synthesis of the ZMO/α-MO nanocomposite was achieved in a one-pot technique by including Ammonium Fluoride (NH_4F) in the reactant mixture [24]. The newly developed ZMO/α-MO nanocomposite with a mixed type morphology was used as an anode material to fabricate Li-half cell [Li | 1 M $LiPF_6$ (EC: EMC) | ZMO/α-MO], and its electrochemical performance was studied systematically.

2. Experimental

2.1. Synthesis of the $ZnMn_2O_4$/α-MnO_2 nanocomposite

The $ZnMn_2O_4$/α-MnO_2 nanocomposite was synthesized *via* a rapid microwave-assisted hydrothermal method, and the complete synthesis process is schematically illustrated in Fig. 1. All the purchased analytical grade reagents were used without further purification. The synthesis process is as follows: 1 mmol of zinc nitrate hexahydrate [Zn

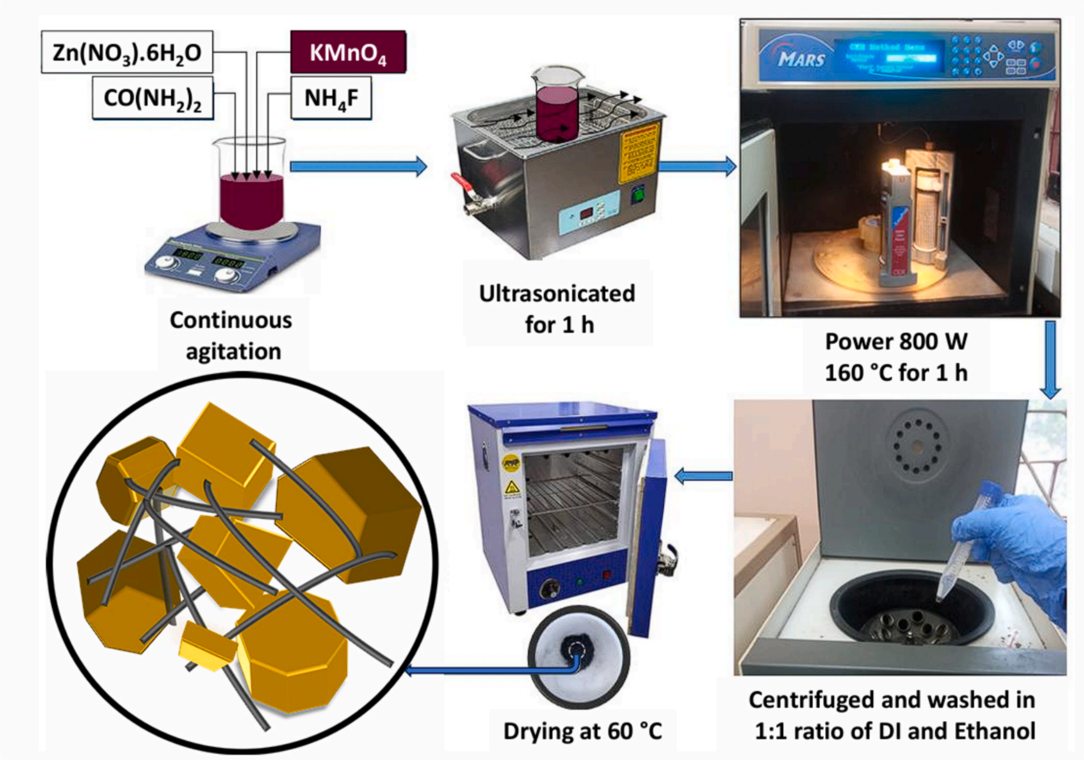

Fig. 1. Schematic illustration of the complete synthesis process for the preparation of $ZnMn_2O_4$/α-MnO_2 nanocomposite by microwave-assisted hydrothermal method.

$(NO_3)_2 \cdot 6H_2O$], 2 mmol of potassium permanganate [$KMnO_4$], 15 mmol of urea [$CO(NH_2)_2$] and 6 mmol ammonium fluoride [NH_4F] were dissolved in 50 mL of deionized water (DI) under continuous stirring for an hour at room temperature, followed by ultrasonication for 30 min. The obtained solution was transferred to a 100 mL Teflon autoclave covered with a composite sleeve, tightly closed, and placed in a CEM-MARS 5 230/60 digestion system. The solution was heated up to 160 °C with a ramp time of 0.5 h, output power set to 800 W, and the temperature was maintained for one hour. After cooling down to room temperature, the obtained precipitate was centrifuged and washed several times with a 1:1 ratio of ethanol and DI water until the pH of the resultant solution was neutralized. Then, the obtained precipitate was dried at 60 °C for 12 h in a hot air oven. Finally, the obtained brown colour powder was ground with a mortar and pestle for further studies.

2.2. *Material characterization*

The as-prepared $ZnMn_2O_4$/α-MnO_2 (ZMO/α-MO) nanocomposite powder sample was extensively characterized using various analytical techniques to confirm its structural, morphological, and chemical properties. X-ray diffraction (XRD) pattern was recorded in the range 5°-80° using a Bruker D8 Advance diffractometer, Bragg-Brentano geometry, and a Lynxeye position-sensitive detector with Cu Kα radiation (1.54 nm). The Raman spectrum was recorded using a WiTeC Alpha 300R Raman imaging microscope with a 532 nm laser source operating at 0.5 mW and the integration time was set to 8 s with 10 accumulations. For Raman measurement, the as-prepared powder sample was dispersed in isopropyl alcohol (IPA) and drop-cast onto a quartz slide. The Fourier-transform infrared (FTIR) spectrum was recorded using a Thermo Scientific Nicolet iS50 Spectrometer in attenuated total reflection (ATR) mode. The morphology of the as-prepared powder sample was recorded in the form of images using Field Emission Scanning Electron Microscopy (FESEM, JEOL JSM-6500F) at an accelerating voltage of 20 kV with a working distance of 10 mm, and an energy-dispersive X-ray spectroscopy (EDX) mapping of each element present in the sample was also recorded using the FE-SEM, JEOL JSM IT800. Further, a High-Resolution Transmission Electron Microscope (HR-TEM), JEOL JEM-2100 model with an acceleration voltage of 200 kV, a point resolution of 0.23 nm, and a lattice resolution of 0.14 nm was used to record the HR-TEM images and selected area electron diffraction (SAED) pattern. The survey and high-resolution X-ray photoelectron spectra (XPS) were recorded under a vacuum of 10^{-9} mbar, at a power of 200 W at an accelerating electron voltage of 13.5 kV using a PHI 5400 ESCA system supplied by Physical Electronics Inc. This system is equipped with a non-monochromatic Al Kα radiation ($h\nu = 1486.7$ eV). The survey spectrum was recorded with a pass energy of 89.45 eV, whereas the high-resolution spectra were recorded with a pass energy of 71.55 eV and the acquired XPS data were processed and fitted using MultiPak v.8.0 software. The N_2 adsorption–desorption isotherm was recorded using a Tristar II 3020 Micromeritics analyser. The specific surface area and pore-size distribution, as well as the pore volume, were evaluated using the Brunauer-Emmett-Teller (BET) and Barrett-Joyner-Halenda (BJH) methods.

2.3. *Electrode preparation*

The working electrode slurry was prepared by mixing ZMO/α-MO nanocomposite as an active material, super P conductive carbon and polyvinylidene fluoride (PVDF) binder in the ratio of 70:20:10 in N-methyl-2-pyrrolidone (NMP) solvent. The resultant slurry was coated over the Cu foil by the doctor blade method and allowed to dry at 80 °C for 12 h in a hot air oven. The prepared ZMO/α-MO coated electrode was cut into circular disks with a diameter of 8 mm, and then the mass loading of active material was measured as 0.66 mg/cm^2. The lithium foil was cut into 10 mm circular discs and was used as a counter and reference electrode. Whatman glass microfiber filter [25] (16 mm in diameter) was used as a separator, and 1 M lithium hexafluorophosphate ($LiPF_6$) in ethylene carbonate (EC) and ethyl methyl carbonate (EMC), (EC: EMC, 1:1 v/v) was used as the electrolyte for the fabrication of Li | 1 M $LiPF_6$ (EC: EMC) | ZMO/α-MO half-cell.

2.4. *Lithium-ion half-cell fabrication and electrochemical measurements*

The CR 2032-coin type lithium-ion half cells were fabricated using lithium metal as the counter electrode and a newly prepared ZMO/α-MO nanocomposite as the working electrode in a high-purity argon (99.999 %) filled glove box (Vigor SciLab glovebox) under a controlled moisture level of about 0.01 ppm, and the Oxygen level was less than 1 ppm. The newly fabricated CR 2032 coin-type half-cells were characterized by measuring cyclic voltammograms (CV), galvanostatic charge/discharge curves, and electrochemical impedance spectra (EIS) using a Biologic BCS 810 electrochemical workstation. The cyclic voltammograms were recorded at a scan rate of 0.1 mVs^{-1}, covering a potential window from 0.01 to 3.0 V (vs. Li/Li$^+$). The galvanostatic charge/discharge measurements were performed within the same potential window to evaluate the capacity retention and rate capability at various current densities (100 mAg^{-1}, 200 mAg^{-1}, 500 mAg^{-1}, 750 mAg^{-1}, and 1000 mAg^{-1}). EIS were recorded over a frequency range from 10 kHz to 1 Hz for the same cell before cycling and after the 50th, 101st, and 251st cycles. All electrochemical measurements were conducted at room temperature.

3. Results and discussions

3.1. *Structural and morphological Characterization of $ZnMn_2O_4$/α-MnO_2 (ZMO/α-MO) nanocomposite*

Fig. 2 shows the XRD pattern of the as-prepared ZMO/α-MO sample along with the JCPDS data of $ZnMn_2O_4$ and α-MnO_2. From Fig. 2, the observed XRD peaks were compared with the JCPDS Card No. 24–1133 (a = b = 5.722 Å and c = 9.236 Å) of $ZnMn_2O_4$ and JCPDS Card No. 44–0141 (a = b = 9.823 Å and c = 2.856 Å) of α-MnO_2. The observed dominant set of sharp and well-defined diffraction peaks at 18.4°, 29.4°, 31.13°, 33.18°, 36.31°, 37.04°, 39.17°, 44.69°, 50.92°, 52.20°, 54.39°, 56.78°, 58.98°, 61.03°, 65.09°, 75.05°, 77.18° and 78.77° were identified as corresponding to the crystalline planes (101), (112), (200), (103), (211), (202), (004), (220), (204), (105), (312), (303), (321), (224), (440), (413), (422) and (404) of polycrystalline phase of tetragonal spinel structured $ZnMn_2O_4$ (ZMO) with space group $I4_1/amd$ [26,27]. Further, the weak and low-intensity XRD peaks observed at 12.8°, 18.0°, 28.8°, 37.5°, and 49.9° were identified as crystalline planes (110), (310), (211), (301), and (411) of the tetragonal α-MnO_2 polycrystalline phase with space group $I4/m$ [28,29]. The crystallite size estimated

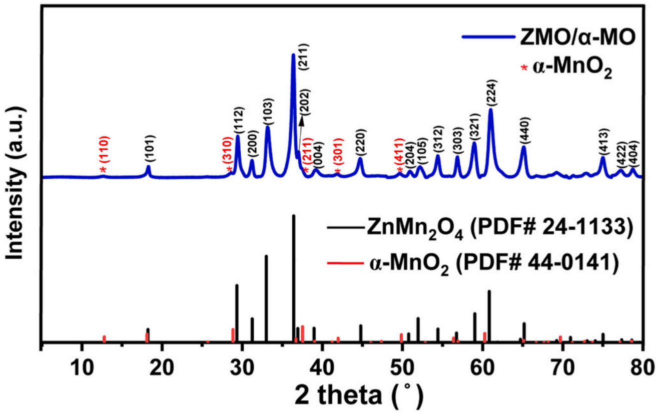

Fig. 2. XRD pattern of as-prepared ZMO/α-MO material along with the JCPDS data of $ZnMn_2O_4$ and α-MnO_2.

through the Williamson-Hall (WH) method using the XRD spectrum is provided in Supplementary Information (Fig. S1). The lower intensity of α-MnO_2 XRD peaks suggests that the ZMO/α-MO composite sample consists of a smaller quantity of α-MnO_2 crystalline phase compared to $ZnMn_2O_4$. From the analysis of the observed XRD pattern, it is concluded that the prepared sample is composed of two different crystalline phases of $ZnMn_2O_4$ and α-MnO_2, and hence, the formation of ZMO/α-MO composite was confirmed. Furthermore, the semi-quantitative phase composition was determined through Rietveld refinement of the XRD pattern (Fig. S2 of the supplementary information), which revealed that the ZMO/α-MO nanocomposite consists of approximately 94 wt% of $ZnMn_2O_4$ and 6 wt% of α-MnO_2.

Fig. 3(a) shows the Raman spectrum of the as-prepared ZMO/α-MO sample. From Fig. 3(a), three prominent peaks were observed at 295.5, 349.4, and 648.8 cm^{-1}. The peak at 648 cm^{-1} can be attributed to the O-Zn-O vibrations in ZnO_4 tetrahedra with A_{1g} symmetry, as well as to the symmetric stretching vibrations of O-Mn-O bonds present in α-MnO_2 [30,31]. The peak at 295.5 cm^{-1} corresponds to the vibrations of E_g Raman mode, whereas the peak at 349.4 cm^{-1} is assigned to the T_{2g} mode of the MnO_6 octahedra in $ZnMn_2O_4$ [31,32]. A slight blue shift was observed for all the Raman peaks of ZMO/α-MO nanocomposite compared to the data from the literature [33]. This may be attributed to phonon confinement effects due to nanocrystalline domains, as well as minor lattice distortions from interfacial interactions between $ZnMn_2O_4$ and the α-MnO_2 phases [34].

Fig. 3(b) shows the FTIR spectrum of the ZMO/α-MO sample. The FTIR peaks were observed at 506.23 cm^{-1} and 620.01 cm^{-1}, which belong to Zn-O vibrations in tetrahedral sites and Mn-O vibrations in octahedral sites from the $ZnMn_2O_4$ spinel structure, respectively [35–37]. The FTIR peaks corresponding to α-MnO_2 were not dominant and distinguishable due to their smaller quantity than $ZnMn_2O_4$ in the ZMO/α-MO nanocomposite, which is consistent with the XRD results. However, a slight shift was observed in the Zn-O vibrational peak at 506.23 cm^{-1} compared to the literature [38]. The Zn–O peak at 506.23 cm^{-1} appeared more intense than the Mn–O peak at 620.01 cm^{-1} from $ZnMn_2O_4$. The slight shift and higher intensity of the Zn-O vibrational peak may be attributed to the contribution of Mn–O vibrations at ~ 522 cm^{-1} from α-MnO_2 [30]. The additional peaks at 2917.81 and 2847 cm^{-1} in the range 2982–2605 cm^{-1} are due to ethanol impurities adsorbed during the washing process, and also due to the adsorbed CO_2 molecules from the atmosphere [30,39]. Thus, Raman and FTIR results further confirm the formation of $ZnMn_2O_4$ and α-MnO_2 in the ZMO/α-MO nanocomposite.

Fig. 4(a-c) presents the FE-SEM images of the as-prepared ZMO/α-MO sample at various magnifications. Fig. 4(d) displays the EDAX mappings of the composite material. The FE-SEM images show the presence of two distinct morphologies: nano-polyhedrons and nanowires. Additionally, the EDAX mapping confirms the presence of Zn, Mn, and O elements in nano-polyhedrons, whereas only Mn and O were detected in the nanowires. This confirms that the nanowires are α-MnO_2 and the nano-polyhedrons are $ZnMn_2O_4$. FE-SEM images clearly show that the quantity of α-MnO_2 nanowires is less compared to the $ZnMn_2O_4$ nano-polyhedrons in the ZMO/α-MO nanocomposite sample, which aligns well with the XRD results. The supplementary Fig. S3 (a) & (b) shows the particle size and diameter distribution of $ZnMn_2O_4$ nano-polyhedrons and α-MnO_2 nanowires, respectively, fitted with a Gaussian distribution. The average particle size of $ZnMn_2O_4$ nano-polyhedrons is found to be ~ 145 nm, and the average diameter of α-MnO_2 nanowires is ~ 23 nm. Thus, the FE-SEM and EDAX mapping of the as-prepared ZMO/α-MO nanocomposite confirms the mixed type morphology of $ZnMn_2O_4$ nano-polyhedrons and α-MnO_2 nanowires.

Fig. 5(a–f) shows the TEM and HR-TEM images at different magnifications and the SAED pattern obtained from the ZMO/α-MO nanocomposite. The TEM images in Fig. 5(a-c) show the mixed morphology of ZMO/α-MO nanocomposite with nano-polyhedrons and nanowires, which agrees with the FE-SEM results. From the HRTEM images in Fig. 5 (d and e), the interplanar spacing of 0.248 nm was measured, which agrees with the d-spacing of the (211) lattice plane of $ZnMn_2O_4$ calculated from XRD data. Hence, it is confirmed that the nano-polyhedrons are $ZnMn_2O_4$, as confirmed from the EDAX mappings. The SAED patterns in Fig. 5(f) were analysed and indexed to lattice planes (204) and (312) of $ZnMn_2O_4$, (200), (310) and (211) of α-MnO_2 phases, which are consistent with the reported literature so far [40,41]. Thus, the HR-TEM and SAED results confirm the presence of two different morphologies and crystalline phases of $ZnMn_2O_4$ and α-MnO_2 nanostructures.

Based on the observed results, the pictorial representation is made for the formation of the $ZnMn_2O_4$ nano-polyhedrons and 1D α-MnO_2 nanowires in the ZMO/α-MO nanocomposite prepared using microwave-assisted hydrothermal synthesis, as shown in Fig. 6. The following possible explanation for the formation of 1D α-MnO_2 nanowires in the ZMO/α-MO nanocomposite is proposed based on the understanding from the available literature. During the hydrothermal synthesis, ammonium fluoride (NH_4F) decomposes at elevated temperatures (~160 °C) to release HF and NH_3, which mildly acidify the local reaction environment [42]. The generated H^+ ions, in the presence of stabilizing cations such as K^+ (from $KMnO_4$) and NH_4^+ (from NH_4F), facilitate the formation of α-MnO_2 with a tunnelled (2 × 2) structure [43,44]. Simultaneously, the fluoride ions (F^-) can coordinate with Zn^{2+} ions, modulating the nucleation pathway and delaying the formation of $ZnMn_2O_4$ [45]. This delay promotes the parallel growth of MnO_2 alongside $ZnMn_2O_4$, enabling the formation of a mixed-type nanocomposite architecture.

The nitrogen adsorption–desorption isotherm of ZMO/α-MO nanocomposite is shown in Fig. 7(a). The specific surface area of the ZMO/α-MO nanocomposite, determined using the Brunauer-Emmett-Teller (BET) method, was found to be 20.42 m^2/g. The nitrogen

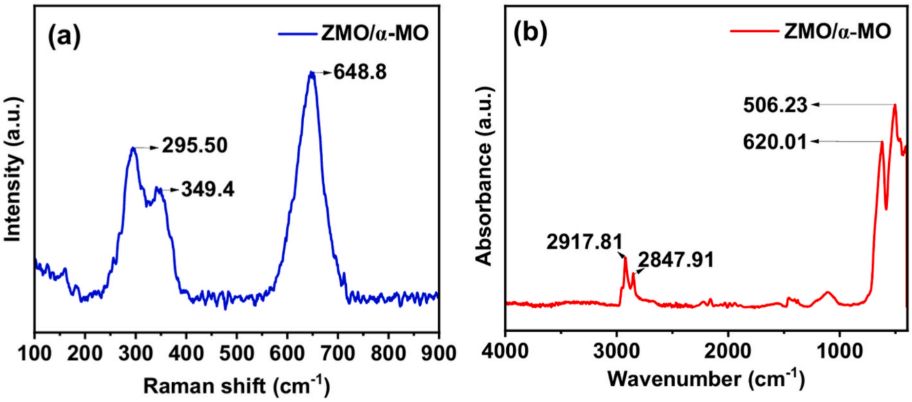

Fig. 3. (a) Raman spectrum and (b) FTIR spectrum of ZMO/α-MO material.

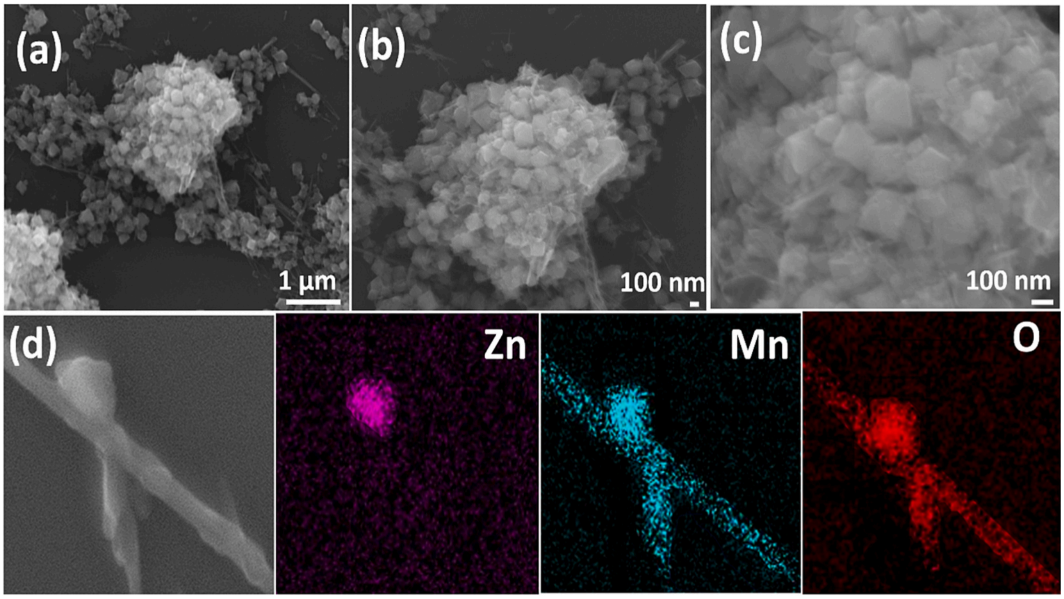

Fig. 4. (a-c) FE-SEM images of as-prepared ZMO/α-MO nanocomposite at different magnifications, (d) Magnified image and corresponding EDAX mappings of Zn, Mn, and O in ZMO/α-MO nanocomposite.

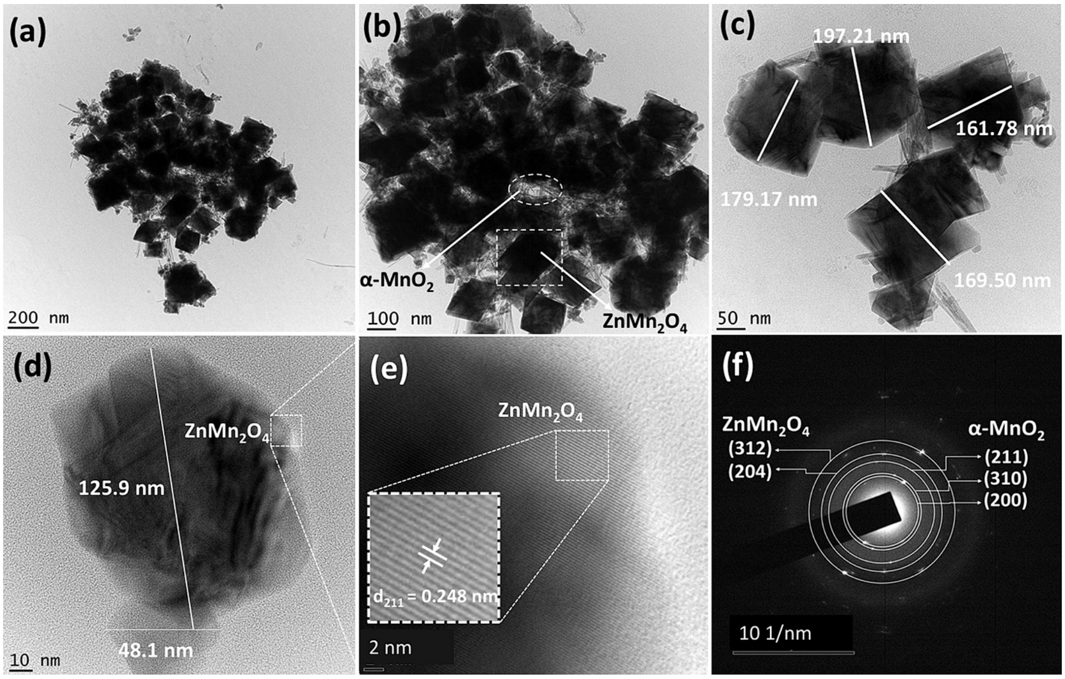

Fig. 5. (a-e) TEM and HR-TEM images of the as-prepared ZMO/α-MO nanocomposite at different magnifications. (f) SAED pattern of ZMO/α-MO nanocomposite.

adsorption–desorption isotherm of ZMO/α-MO nanocomposite showed a type IV isotherm with a wide hysteresis loop within the relative pressure range of 0–1, confirming the mesoporous nature of the sample. The isotherm exhibits an H3-type hysteresis loop, which does not show adsorption saturation at high P/P$_0$, unlike the H1 and H2 types. The H3-type hysteresis observed in the isotherm suggests the presence of slit-shaped pore structures, typically formed between flat surfaces [46–49]. The H3 hysteresis loop may have originated from interparticle voids shaped like slits, formed by the aggregation of nano-polyhedrons and nanowires, as shown in Fig. 7(b). The pore size distribution curve obtained using the Barrett-Joyner-Halenda (BJH) method is shown in the inset of Fig. 7a and the calculated specific pore volume is found to be 0.104 cm^3/g. The effective pore-size distribution falling within the 2–80 nm range, further confirms the mesoporous nature of the slit-shaped pores. As shown in the inset of Fig. 7(a), most of the pores have a diameter of around 50 nm, likely arising from pores formed between the ZMO nano-polyhedrons as confirmed from the HR-TEM image results. The mesoporous structure of ZMO/α-MO nanocomposite, with its high surface area and porosity, may provide advantages such as improved physical contact between electrolyte and nanoparticles, leading to increased ionic and electronic conductivity. The porous structure of the ZMO/α-MO nanocomposite may effectively mitigate volume changes caused by Li$^+$ insertion and extraction, thereby enhancing the cyclic stability of the battery. The observed high porosity and a high surface area of ZMO/α-MO nanocomposite may help to act as an efficient anode material for exhibiting better electrochemical properties.

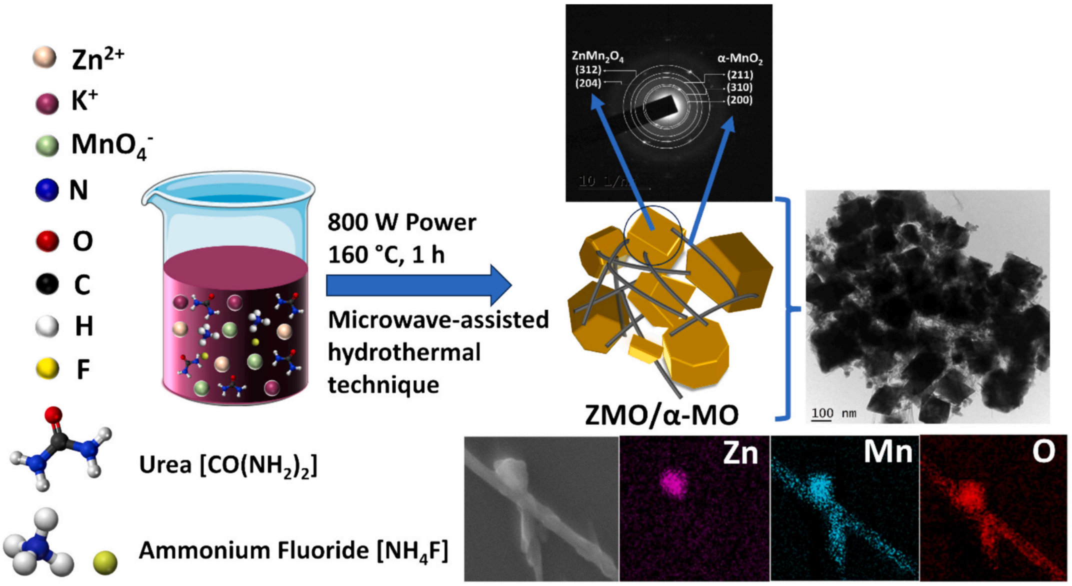

Fig. 6. Pictorial representation made along with observed results for the formation of the $ZnMn_2O_4$ nano-polyhedrons and 1D α-MnO_2 nanowires in the ZMO/α-MO nanocomposite.

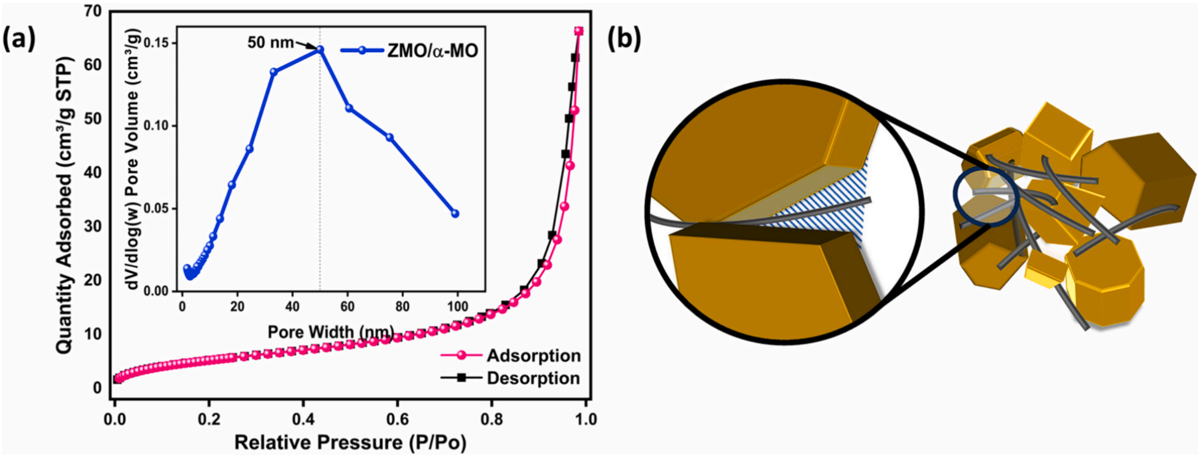

Fig. 7. (a) Nitrogen adsorption–desorption isotherm of ZMO/α-MO nanocomposite. Inset: the pore size distribution curve. (b) Schematic representation of slit-shaped pores of ZMO/α-MO nanocomposite.

Fig. 8 shows the XPS spectra of the ZMO/α-MO nanocomposite. The survey spectrum shown in Fig. 8(a) displays the photo peaks originating from the Mn 2p, Mn 3 s, Mn 3p, Zn 2p, O 1 s, and C 1 s states. The origin of the C 1 s peak is from the adventitious carbon contamination, and it is used for the charge neutralization of XPS data for high-resolution studies by assigning the C–C bond peak at 284.8 eV. In addition, the auger lines from Oxygen (O_{KLL}) and Zinc (Zn_{LMM}) were also observed in the survey spectrum.

In the high-resolution Zn 2p spectrum (Fig. 8(b)), two peaks are observed at 1021.35 eV and 1044.45 eV, which correspond to the Zn $2p_{3/2}$ and Zn $2p_{1/2}$ levels with a spin–orbit splitting of 23.1 eV. The binding energy difference between these peaks confirms that the Zn 2p peak originated from Zn^{2+} in $ZnMn_2O_4$ nanoparticles, by comparing with previously published works [37,50]. Similarly, Mn 2p high-resolution XPS spectrum (Fig. 8(c)) shows two peaks at 642.08 eV and 653.55 eV, which are assigned to Mn 2p3/2 and Mn 2p1/2, respectively. The binding energy difference of 11.47 eV between these peaks confirms that these peaks are from Mn present in the MnO_2, as observed in the work of Bigiani et al. [51].

The observed high-resolution O 1 s spectrum is given in Fig. 8(d). In the O1s spectrum, a peak at 529.9 eV is observed, along with a shoulder peak at 531.9 eV. The prominent peak at 529.9 eV is attributed to the oxygen present in the Zn-O and Mn-O bonds, and the peak at 531.9 eV corresponds to the hydroxyl groups bonded to the metal atoms present in the nanocomposite, which is confirmed by the previous studies [50,51]. In conclusion, XPS analysis further confirms the presence of $ZnMn_2O_4$ and α-MnO_2 in ZMO/α-MO nanocomposite, agreeing with the XRD, FE-SEM, and HR-TEM results.

3.2. Electrochemical performance of ZMO/α-MO nanocomposite

Fig. 9 shows the cyclic voltammograms of the fabricated Li-ion half-cell, recorded in the potential window 0.01–3.0 V (vs. Li/Li^+) at a scan rate of 0.1 mV/s. In the first cathodic scan of the CV curve, three broad peaks at 2.45 V, 1.26 V and 0.73 V, along with a sharp, intense peak at 0.29 V are observed. The first broad peak at 2.45 V corresponds to Lithiation in the α-MnO_2 lattice [52]. The next two broad peaks observed at 1.26 V and 0.72 V are attributed respectively to the reduction of Mn^{3+} from $ZnMn_2O_4$ to Mn^{2+} and electrolyte decomposition, which forms the Solid Electrolyte Interface (SEI) layer [53–55]. The intense, sharp

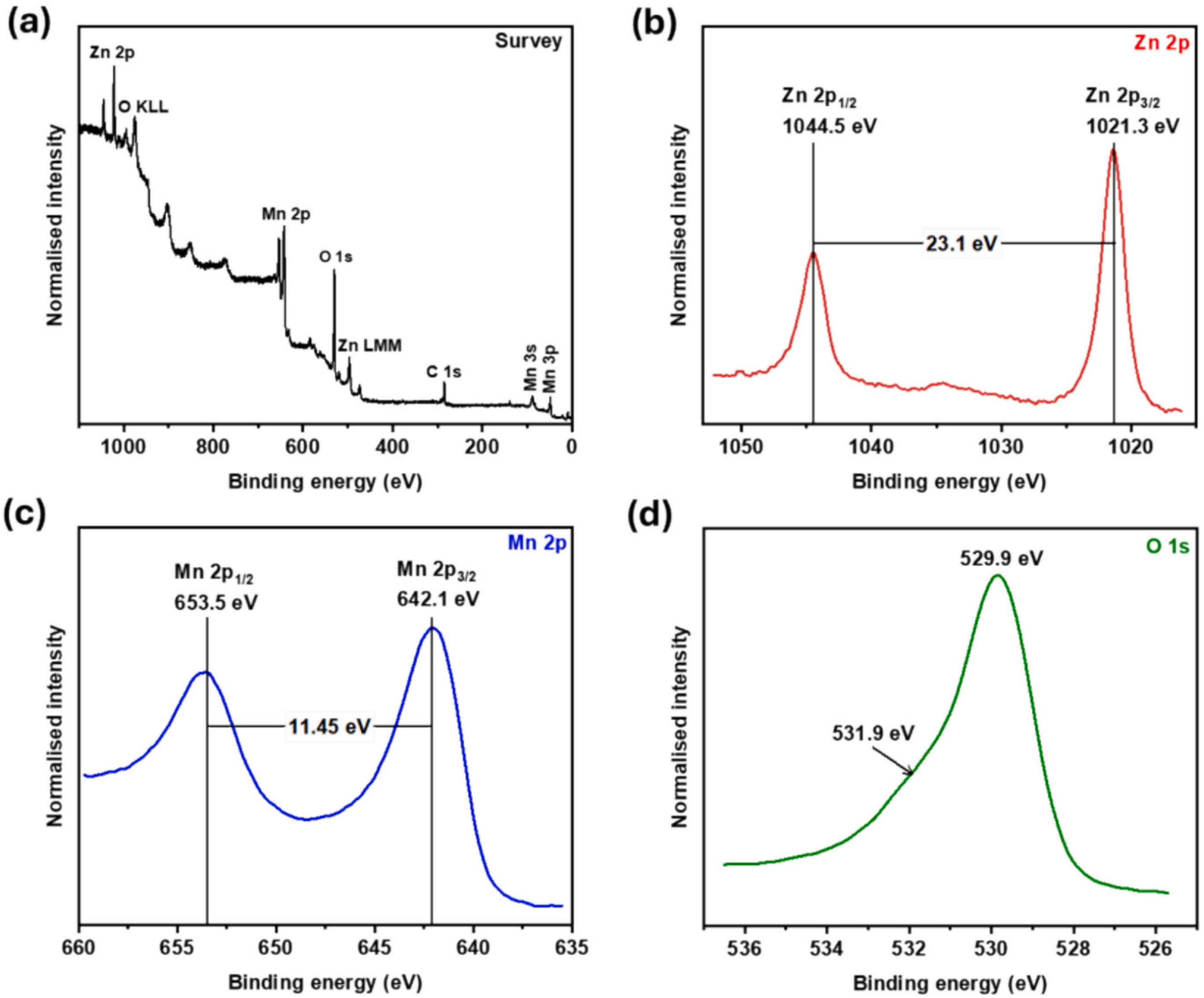

Fig. 8. XPS Spectra of ZMO/α-MO nanocomposite: (a) Survey spectrum, (b) high resolution of Zn 2p spectrum, (c) high resolution of Mn 2p spectrum, and (d) high resolution of O 1 s spectrum.

cathodic peak at 0.29 V is ascribed to the reduction of Mn^{2+} and Zn^{2+} to metallic Mn^0 and Zn^0, along with the formation of Li_2O matrix and Li-Zn alloy, as mentioned in equation (1) [53,55]. During the anodic scan of the first cycle, two broad peaks are observed at 1.19 V and 1.52 V, corresponding to the oxidation of Mn^0 to Mn^{2+} and Zn^0 to Zn^{2+}, respectively. Also, a narrow broadening of the CV curves is observed in the 2.2 – 3.0 V range, which may indicate the oxidation of Mn^{2+} (MnO) to the Mn^{4+} (MnO_2) state as discussed in previous literature [52]. In the case of the second cycle, the observed cathodic scan of the CV curve exhibited only two peaks at 0.49 V and 0.34 V. The broad cathodic peak at 0.49 V corresponds to the reversible reduction reaction of Zn^{2+} and Mn^{2+} to metallic Zn^0 and Mn^0, as represented in equation (3) [13,55]. The sharp peak at 0.34 V is attributed to the reversible reduction of Mn^{4+} to metallic Mn^0 in 1D α-MnO_2, as mentioned in equation (2) [22,52,56,57]. In the subsequent cycles, it was observed that the cathodic and anodic peaks overlapped with minor shifts, implying high reversibility in the chemical reactions as mentioned in equations (2) and (3). When comparing the cathodic peaks at 0.34 V and 0.49 V, the sharp peak at 0.34 V shows better overlap in subsequent cycles, indicating better reaction kinetics of 1-D α-MnO_2. The cathodic peaks observed in the CV profiles at ~ 0.34 V and ~ 0.49 V are attributed to the redox activity of $ZnMn_2O_4$ and α-MnO_2, respectively. Among these, the peak at ~ 0.34 V shows better overlap and sharper intensity across successive cycles, indicating enhanced electrochemical kinetics and the active involvement of 1D α-MnO_2 nanowires. The nearly equal intensity of both peaks suggests comparable redox contributions from both phases. This electrochemical behaviour is further validated by XPS analysis, confirming the surface enrichment of α-MnO_2. These findings suggest that the surface of the composite is likely modified by α-MnO_2 nanowires, providing stable and highly active sites for lithium storage. The observed CV results were consistent with the following chemical reactions [52,53]:

$$ZnMn_2O_4 + 9Li^+ + 9e^- \Rightarrow ZnLi + 2Mn + 4Li_2O \tag{1}$$

$$MnO_2 + 4Li^+ + 4e^- \Leftrightarrow 2Li_2O + Mn \tag{2}$$

$$ZnLi + 2Mn + 3Li_2O \Leftrightarrow ZnO + 2MnO + 7Li^+ + 7e^- \tag{3}$$

In conclusion, CV results confirmed multiple reaction mechanisms occurring, possibly due to the involvement of both $ZnMn_2O_4$ and α-MnO_2 phases during the charging and discharging processes.

Fig. 10 shows the Galvanostatic charge–discharge (GCD) curves of the fabricated Li-ion half-cell using the ZMO/α-MO nanocomposite as

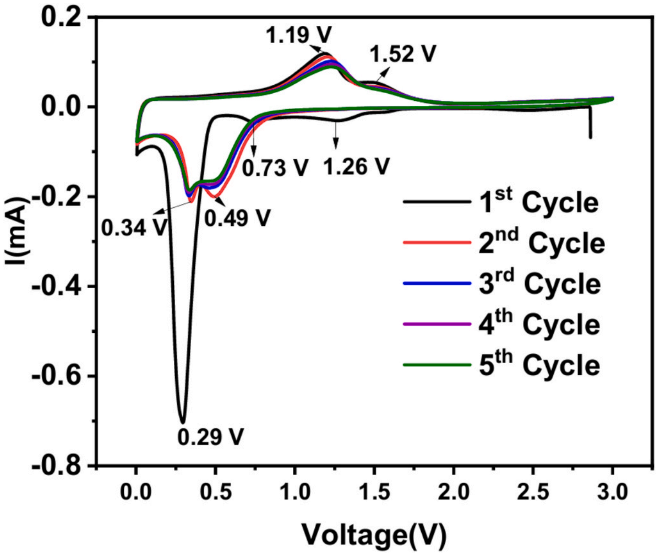

Fig. 9. Cyclic voltammograms of the fabricated Li-ion half-cell using ZMO/α-MO nanocomposite as the anode material.

the anode material up to 100 cycles (1st, 2nd, 3rd, 5th, 10th, 15th, and 100th cycles) at a current density of 100 mAg^{-1} in the potential range 0.01 – 3.0 V (vs. Li/Li^{+}). Based on reactions (1) and (2), and the semi-quantitative phase analysis (94 wt% $ZnMn_2O_4$ and 6 wt% α-MnO_2), the combined theoretical capacity for the first discharge is ~ 1021.44 $mAhg^{-1}$. For the subsequent cycles, based on reactions (2) and (3), the theoretical capacity was calculated to be ~ 810.92 $mAhg^{-1}$. From Fig. 10, it was observed that in the first cycle, the discharge curve exhibited two prominent plateaus in the voltage range of 1.36 – 0.01 V, and the overall discharge capacity delivered was 1346.87 $mAhg^{-1}$. The capacity associated with the first plateau at ~ 1.36 V was ~ 228.37 $mAhg^{-1}$, attributed to the formation of the SEI layer and the reduction of Mn^{3+} to Mn^{2+}, consistent with the CV peaks at 1.26 V and 0.73 V, respectively [54]. Following this, a broader plateau appeared at ~ 0.5 V due to the reduction of $ZnMn_2O_4$ and α-MnO_2, as per reactions (1) and (2), supported by a CV peak more prominently appearing at 0.29 V. In the subsequent charging, the obtained specific charge capacity was 870.72 $mAhg^{-1}$, significantly lower than the first discharge capacity, indicating irreversible Li^{+} consumption in the first discharge [13]. Hence, the coulombic efficiency (CE) for the first cycle was found as only 64.65 %. Although the first charge capacity aligns closely with the theoretical value (~810.92 $mAhg^{-1}$), the second discharge capacity increased to 914.8 $mAhg^{-1}$, exceeding the calculated theoretical value. This enhancement may have resulted from increased participation of redox-active surface sites in α-MnO_2, as supported by the CV profile in the second cycle, where cathodic peaks for $ZnMn_2O_4$ and α-MnO_2 appear with comparable intensity. In the subsequent charging, the second charge capacity was found to decrease to 860.69 $mAhg^{-1}$, which may be attributed to the limited reversibility of certain electrochemical reactions. Hence, for the second cycle, CE was about 94.09 % indicating improved reversibility compared to the first cycle. Additionally, by the 100th cycle, improved electrode stabilization and reversibility led to the reappearance of more well-defined discharge plateaus, indicating enhanced electrochemical kinetics.

The cyclic performance of the fabricated cell with ZMO/α-MO nanocomposite as anode material at different current rates for 251 cycles is presented in Fig. 11. The fabricated cell was first cycled up to 100 cycles to analyse the cycling stability of the ZMO/α-MO nanocomposite as an anode material. During the initial 15 cycles, the capacity drastically dropped to 751.6 $mAhg^{-1}$ due to gradual electrolyte grinding and structural changes occurring for the ZMO/α-MO nanocomposite. However, a gradual increase in capacity was observed after 15 cycles, due to the gradual activation or reactivation of mixed-type morphology and SEI layer formation [58–60]. After around 50 cycles, the ZMO/α-MO nanocomposite showed excellent stability in capacity up to the 100th cycle, suggesting that the activated electrode is showing excellent electrochemical activity [59]. The presence of α-MnO_2 nanowires may have formed a network structure buffering the volume change of pristine

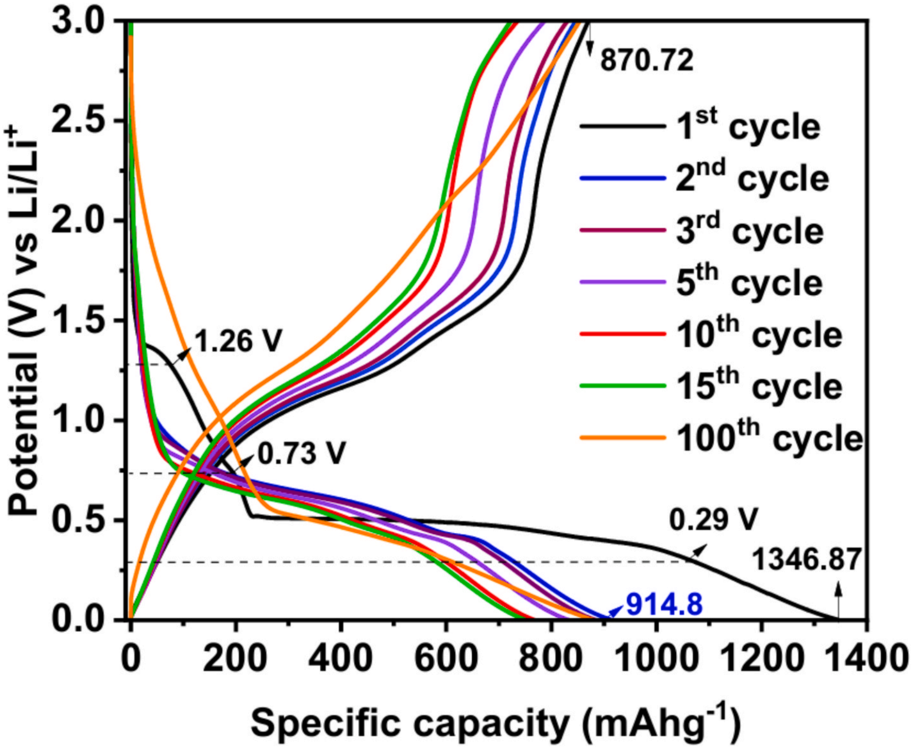

Fig. 10. Galvanostatic charge–discharge curves of Li-ion half-cell using ZMO/α-MO nanocomposite as the anode material up to 100 cycles at 100 mAg^{-1}.

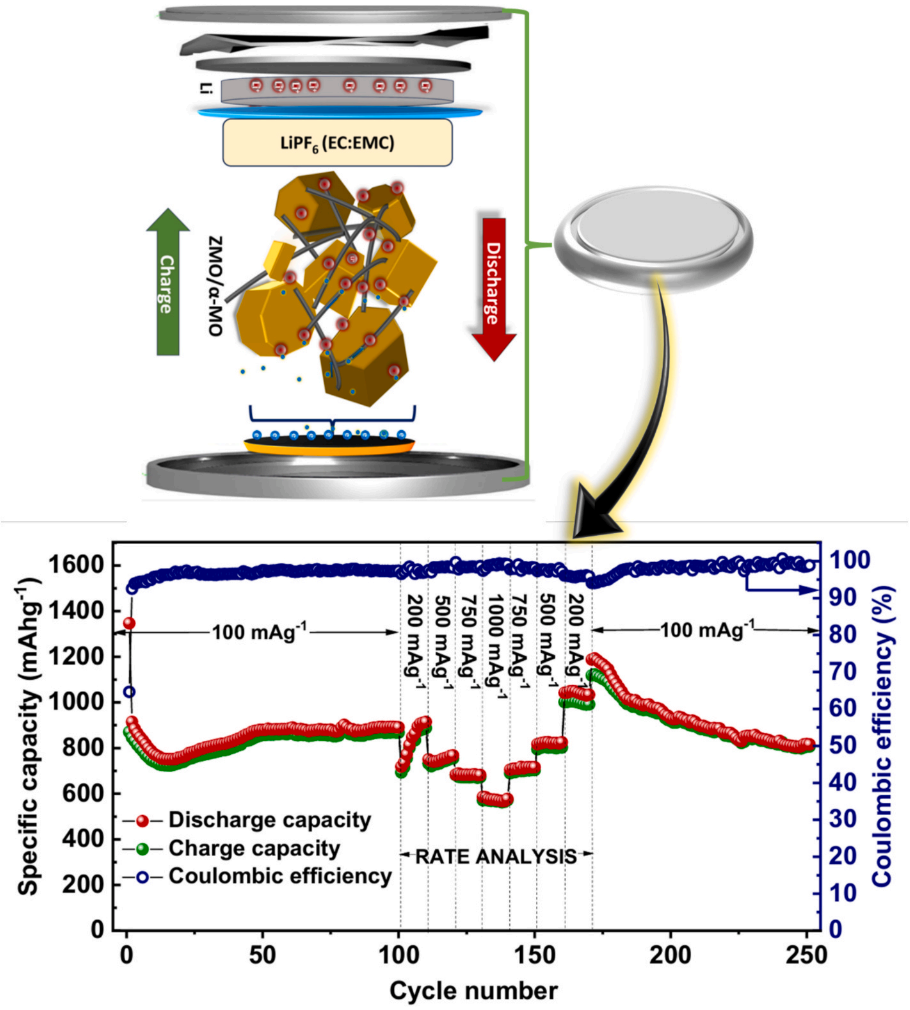

Fig. 11. Cyclic performance of the fabricated Li-ion half-cells with ZMO/α-MO nanocomposite as the anode material up to 251 cycles with different current densities.

$ZnMn_2O_4$ nanostructures and induced additional electrochemically active sites, facilitating lithium-ion diffusion, which becomes more effective after 50 cycles [59]. The newly fabricated cell showed an excellent discharge capacity of 891.6 mAhg^{-1} after 100 cycles at a current rate of 100 mAg^{-1}, demonstrating robust initial cycling performance.

To assess the fabricated cell's ability to withstand higher current rates and its capacity retention after prolonged cycling, rate performance testing was conducted after 100 cycles. Following 100 cycles at 100 mAg^{-1}, the current rate was progressively increased to 200, 500, 750, and 1000 mAg^{-1}, with each rate maintained for 10 cycles, extending the total cycle count to 140. When the current density was increased to 200 mAg^{-1}, the discharge capacity was dropped to 723.9 mAhg^{-1}, followed by a gradual increase to 916.87 mAhg^{-1} in the subsequent cycles, due to the structural arrangement and activation happening again in the mixed-type crystalline phase and material, which may lead to enhanced Li^+ ion diffusion and electrochemical stability as a result of active sites and electrolyte penetration [58]. At higher current densities of 500 mAg^{-1} and 750 mAg^{-1}, the capacity decreased to 753.6 mAhg^{-1} and 678.11 mAhg^{-1}, respectively, highlighting the impact of kinetic limitations on lithium insertion. The reduced lithium storage at these rates is attributed to the shortened lithium-ion diffusion time, which limits the extent of intercalation [61]. However, the coulombic efficiency improved from 98.27 % (120th cycle) to 98.64 % (130th cycle) as the current rate increased from 500 to 750 mAg^{-1}, highlighting the electrode's efficient charge–discharge kinetics and stable electrochemical behaviour. Even at 1000 mAg^{-}1, the electrode maintained a stable capacity of 570.8 mAhg^{-}1 at the 131st cycle, sustaining this performance over the next 10 cycles. Also, the coulombic efficiency further improved to 99.15 % at the 140th cycle, reinforcing the excellent stability and reversibility of ZMO/α-MO nanocomposite electrodes under high-rate cycling conditions. After completing 140 cycles, the same cell was retraced with the decreasing current rates up to the 171st cycle at the current rate of 100 mAg^{-1}, as shown in Fig. 11. It was observed that the discharge and charge capacities increased and were higher than the prior capacities of the respective current rates. The increased capacities may be due to the activation of additional electrochemically active sites and the reorganization of the electrode structure at higher current rates, which may lead to enhanced lithium-ion intercalation. Moreover, the coulombic efficiency gradually decreased, when the current rate was decreased, which may be due to poor reaction kinetics and irreversible side reactions, such as SEI layer reformation by electrolyte decomposition and lithium consumption due to structural degradation. After retracing to 100 mAg^{-1}, a significant increase in capacity to ~ 1117.84 mAhg^{-1} and a decline in coulombic efficiency to 94.1 % was observed, which further suggest the structural and electrochemical modifications that have accompanied the ZMO/α-MO nanocomposite. Thus, ZMO/α-MO nanocomposite showed a hysteresis effect while the current rate was retraced. High-rate cycling from 100 to 140 cycles may have induced serious structural modifications, increased electrolyte penetration, thereby lowering diffusion barriers, and improved contact between the active and electrolyte materials. As a result, enhanced lithium storage capability was observed upon returning to a lower current rate.

However, over extended cycles at current at 100 mAg^{-1}, the discharge capacity stabilized at 808 mAhg^{-1} at the 248th cycle and was observed to increase to 816.2 mAhg^{-1} at 251st cycle slightly, indicating structural and SEI stabilization with minimized degradation and also the coulombic efficiency was observed to be increased to 98.4 %, highlighting excellent reversibility with minimal side reaction and consistent electrochemical performance. The observed slight decrease in capacity from 891.6 mAhg^{-1} at the 100th cycle to 816.2 mAhg^{-1} at the 251st cycle, which could be attributed to continuous activation and SEI layer formation at different current rates. Nevertheless, the newly developed Li-ion half-cell retained its capacity to some extent even after 250 cycles.

As observed in Fig. 11, the discharge capacity initially dropped when the current rate was increased but gradually recovered over subsequent cycles. This trend was evident at 200 and 500 mAg^{-1}, suggesting progressive activation of additional electrochemical active sites and enhanced ionic diffusion. At higher current rates of 750 and 1000 mAg^{-1}, although the capacity increase was less prominent, excellent stability and improved coulombic efficiency were observed. Most notably, upon retracing the current density back to 100 mAg^{-1}, the capacity significantly increased beyond its earlier value (from ~ 891.6 to ~ 1117.84 mAhg^{-1}) and later stabilized, indicating adaptive structural reorganization within the electrode. This behaviour suggests that the ZMO/α-MO nanocomposite not only resists degradation during high-rate cycling but also retains the capability to recover and stabilize its performance, demonstrating a self-regulating or "self-adaptive" electrochemical response. This self-adapting tendency to retain its capacity, observed despite rate changes, is crucial for long-term performance. In addition, the variations in discharge capacities observed at the same current densities (such as 200, 500, and particularly 100 mAg^{-1}) may be due to structural and electrochemical modifications induced during high-rate cycling. The capacity enhancement upon retracing could result from activation of previously inaccessible electrochemical active sites, while the accompanying drop in coulombic efficiency may indicate lithium loss via side reactions such as SEI reformation. This explanation is supported by the observed hysteresis behaviour and evolving efficiency trends over extended cycles [62]. The continuous activation of the electrode helped compensate for the capacity loss caused by SEI layer formation to some extent. This explanation aligns well with the observed decrease in coulombic efficiency during the retracing process. Hence, the newly fabricated Li-half cell, with ZMO/α-MO nanocomposite as the anode material, exhibited a balance between capacity-retention mechanisms and unavoidable degradation effects over extended cycling.

Table 1 compares the cyclic performance of the newly developed ZMO/α-MO nanocomposite with the reported pristine $ZnMn_2O_4$ nanostructures. The discharge capacity of the newly developed ZMO/α-MO nanocomposite as anode material was higher than the reported ones, as shown in Table 1. Hence, the newly developed ZMO/α-MO nanocomposite can be a better anode material for developing high-energy–density and long-cell-life lithium-ion batteries.

Fig. 12 (a) shows the electrochemical impedance spectra of the fabricated Li-ion half-cell before and after n cycles (n = 50, 101, 251) at different current rates. As seen in Fig. 12, the obtained EIS curves exhibit characteristic features such as a semicircle in the high-frequency region representing the ohmic resistance (R_{el}), charge transfer resistance (R_{CT}), and Solid Electrolyte Interface (SEI) resistance (R_{SEI}), and a sloped line in the low-frequency region corresponding to lithium-ion diffusion [54]. The observed electrochemical impedance spectra were fitted using Biologic EC lab software and the equivalent circuits [53] for the lowest $\chi 2$ value (in the range 10^{-3}) for the electrical behaviour of the cell, before and after cycling, as shown in Fig. 12 (b). The obtained R_{el}, R_{CT}, and R_{SEI} values for the developed Li half-cell before and after n cycles (n = 50, 101 & 251) are shown in Table 2. From Table 2, it was observed that Ohmic resistance (R_{el}) gradually increased over prolonged cycling due to electrolyte degradation. Moreover, the charge transfer resistance (R_{CT}) for the fresh cell was found to be ~ 192 Ω and was decreased to ~ 172 Ω, and R_{SEI} was also found to be ~ 172 Ω after the 50th cycle owing to the continuous activation of the ZMO/α-MO nanocomposite electrode and electrolyte degradation during initial cycles. When the current rate was increased from 100 to 200 mAg^{-1} at the 101st cycle, both the R_{CT} and R_{SEI} values were increased and found to be ~ 261 Ω and ~ 300 Ω, respectively, which may be attributed to the existence of a structural change at a sudden higher current rate. Interestingly, there is a significant decline of both R_{CT} and R_{SEI} values, and are found to be ~ 92 Ω and ~ 52 Ω, respectively, after the 251st cycle as a result of enhanced conductivity owing to an increase in electrochemical reaction kinetics in active sites of ZMO/α-MO nanocomposite electrode as well as the evolution of a stable, uniform, and low-resistance SEI layer compared to the initial stages. Thus, the coexistence of the enhanced active sites and a stable SEI layer (lower R_{SEI} than initial) played a vital role in sustaining the ZMO/α-MO nanocomposite electrode performance. Despite the rise in R_{el} over continuous cycling at different current rates, the fabricated Li half-cell with ZMO/α-MO nanocomposite anode electrode retained a substantial capacity of ~ 816.6 mAhg^{-1} at the 251st cycle, owing to the synergistic effect of lower R_{CT} and R_{SEI}. Additionally, it is also observed that Coulombic Efficiency (CE) improved from 97.4 % to 98.8 % at the 100th and 251st cycles, respectively, suggesting fewer parasitic reactions and better utilization of electrochemically active material. Although there was some capacity fading from 891.6 mAhg^{-1} to 816.6 mAhg^{-1} at the 100th cycle to the 251st cycle, the improved CE and superior charge-transfer reaction kinetics effectively compensated for the loss and hence the newly developed Li-ion half-cell with ZMO/α-MO nanocomposite anode electrode could be a potential candidate to ensure excellent long-term cycling performance for Li-ion batteries.

4. Conclusions

The newly synthesized $ZnMn_2O_4$/α-MnO_2 (ZMO/α-MO) nanocomposite *via* a one-pot, organic solvent-free, microwave-assisted hydrothermal method exhibits a promising nanostructured architecture as an anode material for high-performance lithium-ion batteries. Formation of a dominant tetragonal phase of $ZnMn_2O_4$ along with a minor

Table 1

A comparison of electrochemical performances of the developed ZMO/α-MO nanocomposite along with those reported in prior literature.

Morphology	Method	Current Density (mAg^{-1})	Cycle number	Final capacity (mAhg^{-1})	Ref.
Nanocrystals	Polymer-pyrolysis- method	100	50	569	[63]
Nanowires	Solid-state reaction	100	40	650	[64]
Nanoparticles	Hydrothermal process	100	90	716	[65]
Mesoscale tubular	Hydrothermal process	100	100	784.3	[66]
Flowerlike microsphere	Solvothermal process	100	120	662	[67]
Porous nanospheres	Microemulsion method	100	120	810	[26]
Crumbled nanosheets	Electrospinning method	100	500	461	[68]
Porous rugby balls	Hydrothermal process	100	100	614	[69]
Nano peanuts	Solvothermal process	100	200	812	[70]
Mixed morphology of Nanostructures	Microwave-assisted-hydrothermal synthesis	100	100	891.6	Present Work

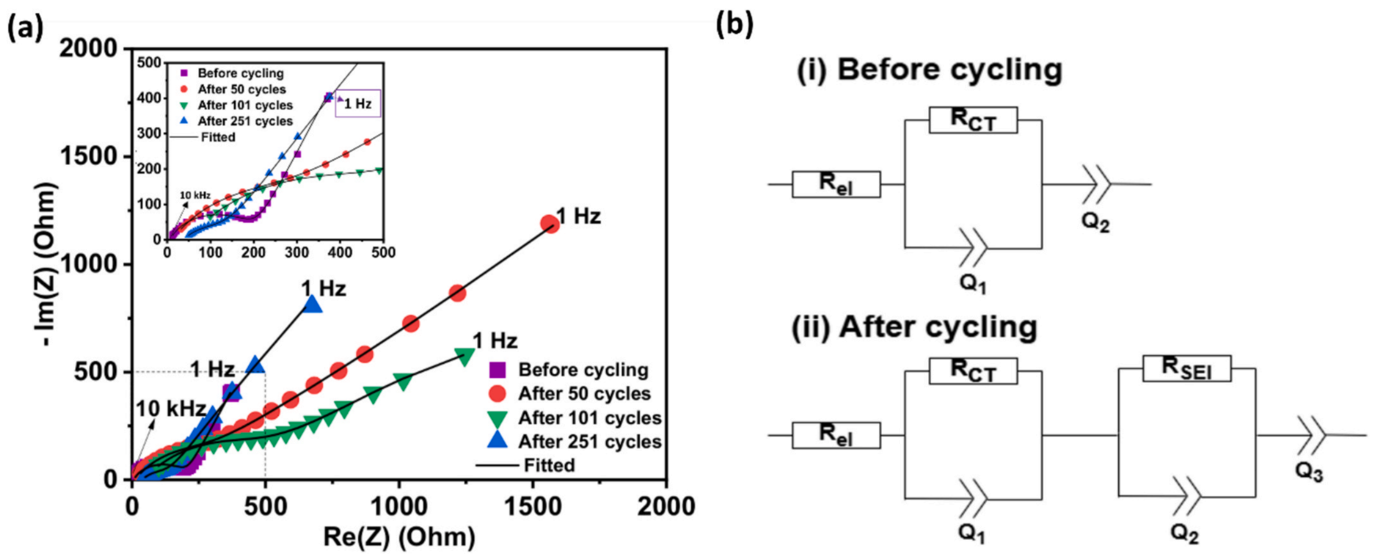

Fig. 12. (a) Electrochemical impedance spectra (EIS) of the fabricated Li half-cell before and after n cycles (n = 50, 101, 251) at 100 and 200 mAg^{-1} current rates. (b) shows the corresponding equivalent circuits for the cell before and after cycling.

Table 2
Electrochemical Impedance Parameters at Different Cycling Stages of the newly developed Li-ion half-cell with ZMO/α-MO nanocomposite as anode.

Cycle stage	R_{el} (Ω)	R_{CT} (Ω)	R_{SEI} (Ω)
Before cycling	7	192	–
After 50 cycles	8	172	172
After 101 cycles	19	261	300
After 251 cycles	39	92	52

tetragonal α-MnO_2 crystalline phase in the $ZnMn_2O_4$/α-MnO_2 nanocomposite was confirmed by XRD analysis, further supported by Rietveld refinement, which revealed a phase composition of approximately 94 wt% of $ZnMn_2O_4$ and 6 wt% of α-MnO_2. Heterogeneous hybrid morphology composed of $ZnMn_2O_4$ nano-polyhedrons and 1D α-MnO_2 nanowires was confirmed from the analysis of FE-SEM, HR-TEM and EDAX results. Structure, elemental compositions and oxidation states in the as-prepared $ZnMn_2O_4$/α-MnO_2 nanocomposite were confirmed from the analysis of Raman, FTIR, and XPS results, respectively. The specific surface area of the as-prepared ZMO/α-MO nanocomposite, determined *via* the Brunauer–Emmett–Teller (BET) method, was found to be 20.42 m^2g^{-1}. The average pore width, calculated using the Barrett–Joyner–Halenda (BJH) method, was approximately 50 nm, indicating a high surface area and a suitable pore size favourable for efficient lithium-ion insertion. The fabricated Li-ion half-cell with ZMO/α-MO nanocomposite as the anode electrode delivered a high discharge capacity of 891.6 mAhg^{-1} at the 100th cycle at 100 mAg^{-1}, along with excellent rate capability and improved coulombic efficiency (CE) at higher current densities. Although an initial fluctuation in capacity and CE was observed upon retracing to 100 mAg^{-1}, the cell demonstrated a stabilized performance by around the 248th cycle. Analysis of the electrochemical results of cyclic voltammetry and electrochemical impedance spectroscopy (EIS), revealed improved electrode kinetics and stable SEI layer conductivity during prolonged cycling. These results highlight that the synergistic integration of $ZnMn_2O_4$ nano-polyhedrons with 1D α-MnO_2 nanowires significantly enhances lithium-ion storage capabilities, rate adaptability, and long-term cycling stability by mitigating the volume expansion. Hence, the electrochemical performance of the newly developed ZMO/α-MO nanocomposite demonstrates its strong potential for next-generation high-performance lithium-ion battery anode applications.

Funding.

B.C has received research fellowship support from Pondicherry University. N.S. has received UGC-BSR Faculty Fellowship support from the UGC, Government of India (No. F.18–1/2011(BSR), Date: 07–03-2019).

CRediT authorship contribution statement

Bharath Chandran: Writing – original draft, Visualization, Methodology, Investigation, Formal analysis, Data curation, Conceptualization. **Reshma S. Babu:** Writing – review & editing, Methodology, Investigation, Data curation. **Prasad Gonugunta:** Data Curation, Supervision, Writing – review & editing, Methodology, Investigation, Formal analysis. **O. Padmaraj:** Writing – review & editing, Visualization, Validation, Formal analysis. **Thamayanthi Panneerselvam:** Resources, Methodology. **R. Murugan:** Resources. **Gangineni Ramesh Babu:** Writing – review & editing, Supervision. **Ruud Hendrikx:** Methodology, Investigation, Data curation. **Peyman Taheri:** Resources, Formal analysis, Writing – review & editing. **Arjan Mol:** Writing – review & editing, Resources, Formal analysis, Data curation. **N. Satyanarayana:** Writing – review & editing, Validation, Supervision, Resources, Project administration, Funding acquisition, Formal analysis, Data curation. **Prasaanth Ravi Anusuyadevi:** Writing – review & editing, Visualization, Supervision, Project administration, Formal analysis, Data curation, Conceptualization.

Declaration of competing interest

The authors declare that they have no known competing financial interests or personal relationships that could have appeared to influence the work reported in this paper.

Acknowledgements

The authors are grateful to the Central Instrumentation Facility (CIF), Pondicherry University, for providing access to various characterization facilities. N.S. acknowledges the University Grants Commission (UGC), Government of India, for awarding the UGC-BSR Faculty Fellowship (No. F.18-1/2011(BSR), dated 07-03-2019). The authors also express their sincere thanks to DST-FIST Phase-II for supporting the GIXRD facility in the Department of Physics, Pondicherry University. B. C. acknowledges Pondicherry University for providing the research fellowship.

Appendix A. Supplementary data

Supplementary data to this article can be found online at https://doi.org/10.1016/j.apsusc.2025.164175.

Data availability

Data will be made available on request.

References

[1] L. Lu, X. Han, J. Li, J. Hua, M. Ouyang, A review on the key issues for lithium-ion battery management in electric vehicles, J. Power Sources 226 (2013) 272–288, https://doi.org/10.1016/j.jpowsour.2012.10.060.

[2] D. Kasprzak, C.C. Mayorga-Martinez, M. Pumera, Sustainable and Flexible Energy Storage Devices: a Review, Energy Fuel 37 (2023) 74–97, https://doi.org/10.1021/acs.energyfuels.2c03217.

[3] J.W. Choi, D. Aurbach, Promise and reality of post-lithium-ion batteries with high energy densities, Nat. Rev. Mater. 1 (2016) 16013, https://doi.org/10.1038/natrevmats.2016.13.

[4] R.M. Humana, M.G. Ortiz, J.E. Thomas, S.G. Real, M. Sedlarikova, J. Vondrák, A. Visintin, Preparation and Characterization of Graphite Anode for Lithium Ion Batteries, ECS Trans. 63 (2014) 91–97, https://doi.org/10.1149/06301.0091ecst.

[5] J.-M. Tarascon, M. Armand, Issues and challenges facing rechargeable lithium batteries, Nature 414 (2001) 359–367, https://doi.org/10.1038/35104644.

[6] C. Zhao, S. Yao, C. Li, Y. An, S. Zhao, X. Sun, K. Wang, X. Zhang, Y. Ma, Recent advances in transition metal oxides as anode materials for high-performance lithium-ion capacitors, Chem. Eng. J. 497 (2024), https://doi.org/10.1016/j.cej.2024.154535.

[7] K. Ullah, N. Shah, R. Wadood, B.M. Khan, W.C. Oh, Recent trends in graphene based transition metal oxides as anode materials for rechargeable lithium-ion batteries, Nano Trends 1 (2023) 100004, https://doi.org/10.1016/j.nwnano.2023.100004.

[8] Y. Zhao, X. Li, B. Yan, D. Xiong, D. Li, S. Lawes, Recent Developments and Understanding of Novel Mixed Transition-Metal Oxides as Anodes in Lithium Ion Batteries (2016), https://doi.org/10.1002/aenm.201502175.

[9] Y. Zhu, X. Liao, H. Qiu, S. An, Y. Zhang, W. He, Mixed metals oxides with strong synergetic electrochemistry as battery-type electrodes for ultrafast energy storage, J. Alloys Compd. 848 (2020), https://doi.org/10.1016/j.jallcom.2020.156395.

[10] S. Yuvaraj, R.K. Selvan, Y.S. Lee, An overview of AB_2O_4- and A_2BO_4-structured negative electrodes for advanced Li-ion batteries, RSC Adv. 6 (2016) 21448–21474, https://doi.org/10.1039/c5ra23503k.

[11] R.S. Babu, E. Madai, D.S. Nair, P. Gonugunta, S.M. Armaki, R. Hendrikx, T. Panneerselvam, R. Murugan, V.V.R.K. Kumar, P. Taheri, A. Mol, N. Satyanarayana, P.R. Anusuyadevi, Effect of synthesis conditions on morphology, surface chemistry and electrochemical performance of nickel ferrite nanoparticles for lithium-ion battery applications, J. Mater. Sci. Mater. Electron. 36 (2025) 1–23, https://doi.org/10.1007/S10854-025-14886-W/METRICS.

[12] C. Liang, J. Chen, K. Yu, W. Jin, $ZnMn_2O_4$ spheres anchored on jute porous carbon for use as a high-performance anode material in lithium-ion batteries, J. Alloys Compd. 878 (2021), https://doi.org/10.1016/j.jallcom.2021.160445.

[13] D. Cai, D. Wang, H. Huang, X. Duan, B. Liu, L. Wang, Y. Liu, Q. Li, T. Wang, Rational synthesis of $ZnMn_2O_4$ porous spheres and graphene nanocomposite with enhanced performance for lithium-ion batteries, J Mater Chem A Mater 3 (2015) 11430–11436, https://doi.org/10.1039/c5ta00539f.

[14] C. Feng, W. Wang, X. Chen, S. Wang, Z. Guo, Synthesis and electrochemical properties of $ZnMn_2O_4$ anode for lithium-ion batteries, Electrochim. Acta 178 (2015) 847–855, https://doi.org/10.1016/j.electacta.2015.08.070.

[15] Y. Zhang, P. Zhang, Y. Xu, X. Song, H. Wang, T. Ma, Synthesis of pomegranate-shaped micron $ZnMn_2O_4$ with enhanced lithium storage capability, J. Materiomics 7 (2021) 699–707, https://doi.org/10.1016/j.jmat.2021.01.005.

[16] J. Chen, F. Cheng, Combination of lightweight elements and nanostructured materials for batteries, Acc. Chem. Res. 42 (2009) 713–723, https://doi.org/10.1021/ar800229g.

[17] Z. Zheng, Y. Cheng, X. Yan, R. Wang, P. Zhang, Enhanced electrochemical properties of graphene-wrapped $ZnMn_2O_4$ nanorods for lithium-ion batteries, J Mater Chem A Mater 2 (2014) 149–154, https://doi.org/10.1039/c3ta13511j.

[18] S. Cheng, Q. Ru, Y. Gao, M. Zhen, F. Chen, L. Wei, F.C.C. Ling, Anionic defect-enriched $ZnMn_2O_4$ nanorods with boosting pseudocapacitance for high-efficient and durable Li/Na storage, Chem. Eng. J. 406 (2021), https://doi.org/10.1016/j.cej.2020.126133.

[19] Z. Bai, N. Fan, C. Sun, Z. Ju, C. Guo, J. Yang, Y. Qian, Facile synthesis of loaf-like $ZnMn_2O_4$ nanorods and their excellent performance in Li-ion batteries, Nanoscale 5 (2013) 2442–2447, https://doi.org/10.1039/c3nr33211j.

[20] J. Zia, E.S. Aazam, U. Riaz, Facile synthesis of MnO_2 nanorods and $ZnMn_2O_4$ nanohexagons: a comparison of microwave-assisted catalytic activity against 4-nitrophenol degradation, J. Mater. Res. Technol. 9 (2020) 9709–9719, https://doi.org/10.1016/j.jmrt.2020.06.048.

[21] E. Umeshbabu, M. Satyanarayana, G. Karkera, A. Pullamsetty, P. Justin, Hierarchical α-MnO_2 nanowires as an efficient anode material for rechargeable lithium-ion batteries, Mater. Adv. 3 (2022) 1642–1651, https://doi.org/10.1039/d1ma00755f.

[22] H.M. Kim, B.C. Cha, D.W. Kim, High-Rate One-Dimensional α-MnO_2 Anode for Lithium-Ion Batteries: Impact of Polymorphic and Crystallographic Features on Lithium Storage, Nanomaterials 13 (2023), https://doi.org/10.3390/nano13202808.

[23] J. Chen, Y. Wang, X. He, S. Xu, M. Fang, X. Zhao, Y. Shang, Electrochemical properties of MnO_2 nanorods as anode materials for lithium ion batteries, Electrochim. Acta 142 (2014) 152–156, https://doi.org/10.1016/j.electacta.2014.07.089.

[24] Y. Cao, Z. Wei, J. He, J. Zang, Q. Zhang, M. Zheng, Q. Dong, α-MnO_2 nanorods grown in situ on graphene as catalysts for Li-O_2 batteries with excellent electrochemical performance, Energy, Environ. Sci. 5 (2012) 9765–9768, https://doi.org/10.1039/c2ee23475k.

[25] B. Kurc, M. Pigłowska, An influence of temperature on the lithium ions behavior for starch-based carbon compared to graphene anode for LIBs by the electrochemical impedance spectroscopy (EIS), J. Power Sources 485 (2021), https://doi.org/10.1016/j.jpowsour.2020.229323.

[26] X. Chen, Y. Zhang, H. Lin, P. Xia, X. Cai, X. Li, X. Li, W. Li, Porous $ZnMn_2O_4$ nanospheres: Facile synthesis through microemulsion method and excellent performance as anode of lithium ion battery, J. Power Sources 312 (2016) 137–145, https://doi.org/10.1016/j.jpowsour.2016.02.056.

[27] X. Zhu, J. Quan, J. Huang, Z. Ma, Y. Chen, D. Zhu, C. Ji, D. Li, A new approach to improve the electrochemical performance of $ZnMn_2O_4$ through a charge compensation mechanism using the substitution of Al^{3+} for Zn^{2+}, RSC Adv. 8 (2018) 7361–7368, https://doi.org/10.1039/c8ra00310f.

[28] H. Wang, D. Qian, Z. Lu, Y. Li, R. Cheng, W. Zhang, Facile synthesis of α-MnO_2 nanorods and their electrochemical performances, J. Cryst. Growth (2007), https://doi.org/10.1016/j.jcrysgro.2007.01.034.

[29] J. Luo, H.T. Zhu, H.M. Fan, J.K. Liang, H.L. Shi, G.H. Rao, J.B. Li, Z.M. Du, Z. X. Shen, Synthesis of single-crystal tetragonal α-MnO_2 nanotubes, J. Phys. Chem. C 112 (2008) 12594–12598, https://doi.org/10.1021/jp8052967.

[30] E. Hastuti, A. Subhan, P. Amonpattaratkit, M. Zainuri, S. Suasmoro, The effects of Fe-doping on MnO_2: phase transitions, defect structures and its influence on electrical properties, RSC Adv. 11 (2021) 7808–7823, https://doi.org/10.1039/d0ra10376d.

[31] E.S. Guillén-López, F. López-Urías, E. Muñoz-Sandoval, M. Courel-Piedrahita, M. Sanchez-Tizapa, H. Guillén-Bonilla, V.M. Rodríguez-Betancourtt, O. Blanco-Alonso, A. Guillén-Bonilla, J.P. Morán-Lázaro, High performance isopropanol sensor based on spinel $ZnMn_2O_4$ nanoparticles, Mater. Today Commun. 26 (2021), https://doi.org/10.1016/j.mtcomm.2021.102138.

[32] H. Li, B. Song, W.J. Wang, X.L. Chen, Facile synthesis, thermal, magnetic, Raman characterizations of spinel structure $ZnMn_2O_4$, Mater. Chem. Phys. 130 (2011) 39–44, https://doi.org/10.1016/j.matchemphys.2011.04.072.

[33] C. Shamitha, T. Senthil, L. Wu, B.S. Kumar, S. Anandhan, Sol–gel electrospun mesoporous $ZnMn_2O_4$ nanofibers with superior specific surface area, J. Mater. Sci. Mater. Electron. 28 (2017) 15846–15860, https://doi.org/10.1007/s10854-017-7479-0.

[34] S.V. Koniakhin, O.I. Utesov, A.G. Yashenkin, Raman peak shift and broadening in crystalline nanoparticles with lattice impurities, Diam. Relat. Mater. 146 (2024), https://doi.org/10.1016/j.diamond.2024.111182.

[35] P. Deva, S. Ravi, C. Manoharan, Synthesis of mesoporous structured $ZnMn_2O_4$ nanoparticles as electrode for supercapacitor application, Emergent Mater (2024), https://doi.org/10.1007/s42247-024-00759-1.

[36] S. Aouini, A. Bardaoui, A.M. Ferraria, D.M.F. Santos, R. Chtourou, $ZnMn_2O_4$ Nanopyramids Fabrication by Hydrothermal Route: effect of Reaction Time on the Structural, Morphological, and Electrochemical Properties, Energies (basel) 15 (2022), https://doi.org/10.3390/en15249352.

[37] P. Zhang, X. Li, Q. Zhao, S. Liu, Synthesis and optical property of one-dimensional spinel $ZnMn_2O_4$ nanorods, Nanoscale Res. Lett. 6 (2011), https://doi.org/10.1186/1556-276X-6-323.

[38] H. Barkhordari, H. Heydari, A. Nosrati, J. Mohammadi, Facile synthesis of $ZnMn_2O_4$ nanosheets via cathodic electrodeposition: characterization and supercapacitor behavior studies, Ionics (kiel) 25 (2019) 275–285, https://doi.org/10.1007/s11581-018-2565-8.

[39] P.E. Saranya, S. Selladurai, Efficient electrochemical performance of $ZnMn_2O_4$ nanoparticles with rGO nanosheets for electrodes in supercapacitor applications, J. Mater. Sci. Mater. Electron. 29 (2018) 3326–3339, https://doi.org/10.1007/s10854-017-8268-5.

[40] L. Dong, J. Hao, H. Liu, W. Shi, J. Yang, J. Lian, Three-Dimensional $ZnMn_2O_4$ Nanoparticles/Carbon Cloth Anodes for High-Performance Flexible Lithium-Ion Batteries, ChemistrySelect 5 (2020) 2372–2378, https://doi.org/10.1002/slct.202000037.

[41] E. Hastuti, A. Subhan, P. Amonpattaratkit, M. Zainuri, T. Triwikantoro, S. Suasmoro, Oxidation state, local structure distortion, and defect structure analysis of Cu doped α-MnO_2 correlated to conductivity and dielectric properties, Heliyon 8 (2022), https://doi.org/10.1016/j.heliyon.2022.e11459.

[42] E.G. Rakov, E.I. Mel`nichenko, The Properties and Reactions of ammonium Fluorides, Russ. Chem. Rev. 53 (9) (1984) 851–869, https://doi.org/10.1070/RC1984v053n09ABEH003126.

[43] X. Huang, D. Lv, H. Yue, A. Attia, Y. Yang, Controllable synthesis of α- and β-MnO_2: Cationic effect on hydrothermal crystallization, Nanotechnology 19 (2008), https://doi.org/10.1088/0957-4484/19/22/225606.

[44] X. Hu, S. Zhu, H. Huang, J. Zhang, Y. Xu, Controllable synthesis and characterization of α-MnO_2 nanowires, J. Cryst. Growth 434 (2016) 7–12, https://doi.org/10.1016/j.jcrysgro.2015.10.020.

[45] H. Du, Y. Wang, H. Yuan, L. Jiao, Facile Synthesis and High Capacitive Performance of 3D Hierarchical Ni(OH)$_2$ Microspheres, Electrochim. Acta 196 (2016) 84–91, https://doi.org/10.1016/j.electacta.2016.02.190.

[46] Y. Yamaguchi, R. Aono, E. Hayashi, K. Kamata, M. Hara, Template-free synthesis of mesoporous β-MnO$_2$ nanoparticles: Structure, formation mechanism, and catalytic properties, ACS Appl. Mater. Interfaces 12 (2020) 36004–36013, https://doi.org/10.1021/acsami.0c08043.

[47] M. Thommes, K. Kaneko, A.V. Neimark, J.P. Olivier, F. Rodriguez-Reinoso, J. Rouquerol, K.S.W. Sing, Physisorption of gases, with special reference to the evaluation of surface area and pore size distribution (IUPAC Technical Report), Pure Appl. Chem. 87 (2015) 1051–1069, https://doi.org/10.1515/pac-2014-1117.

[48] K.S.W. Sing, Reporting Physisorption Data for Gas/Solid Systems with special Reference to the Determination of Surface Area and Porosity. IUPAC Commission on Colloid and Surface Chemistry Including Catalysis, Pure Appl. Chem. 57 (1985) 603–619, https://doi.org/10.1351/pac198557040603.

[49] B.D. Zdravkov, J.J. Čermák, M. Šefara, J. Janků, Pore classification in the characterization of porous materials: a perspective, Cent. Eur. J. Chem. 5 (2007) 385–395, https://doi.org/10.2478/s11532-007-0017-9.

[50] I.V. Ivanova, N.A. Zaitseva, R.F. Samigullina, T.I. Krasnenko, Solid-state synthesis of ZnMn$_2$O$_4$ spinel: Sequence of phase transformations, thermal stability, localization and charge state of manganese ions in the intermediate and final reaction products, Solid State Sci. 136 (2023), https://doi.org/10.1016/j.solidstatesciences.2023.107110.

[51] L. Bigiani, C. Maccato, A. Gasparotto, C. Sada, E. Bontempi, D. Barreca, Plasma-assisted chemical vapor deposition of f-doped MnO$_2$ nanostructures on single crystal substrates, Nanomaterials 10 (2020) 1–13, https://doi.org/10.3390/nano10071335.

[52] Y.C. Tsai, C.T. Kuo, S.F. Liu, Y.T. Lee, T.R. Yew, Effect of Different Electrolytes on MnO$_2$ Anodes in Lithium-Ion Batteries, J. Phys. Chem. C 125 (2021) 1221–1233, https://doi.org/10.1021/acs.jpcc.0c09022.

[53] Z. Zhao, G. Tian, A. Sarapulova, V. Trouillet, Q. Fu, U. Geckle, H. Ehrenberg, S. Dsoke, Elucidating the energy storage mechanism of ZnMn$_2$O$_4$ as promising anode for Li-ion batteries, J Mater Chem A Mater 6 (2018) 19381–19392, https://doi.org/10.1039/c8ta06294c.

[54] P. Zhou, L. Zhong, Z. Liu, M. Liu, T. Zhou, Y. Zhao, X. Lai, J. Bi, D. Gao, Porous ZnMn$_2$O$_4$ hollow microrods: Facile construction and excellent electrochemical performances for lithium-ion batteries, Appl. Surf. Sci. 578 (2022) 152087, https://doi.org/10.1016/j.apsusc.2021.152087.

[55] N. Wang, X. Ma, H. Xu, L. Chen, J. Yue, F. Niu, J. Yang, Y. Qian, Porous ZnMn$_2$O$_4$ microspheres as a promising anode material for advanced lithium-ion batteries, Nano Energy 6 (2014) 193–199, https://doi.org/10.1016/j.nanoen.2014.04.001.

[56] K. Kasiviswanathan, K. Lakshmanan, S. Chenrayan, C. Woo Lee, B. Rangasamy, K. Vediappan, Electrochemically Induced Borate Allotropes for Expedite Charge Transfer in Lithium-Ion Batteries and Hydroxyl Ion Capture Activity in Flexible Pseudocapacitor, Batter Supercaps 6 (2023). Doi: 10.1002/batt.202200449.

[57] L. Feng, Z. Xuan, H. Zhao, Y. Bai, J. Guo, C. Wei Su, X. Chen, MnO$_2$ prepared by hydrothermal method and electrochemical performance as anode for lithium-ion battery, Nanoscale Res Lett 9 (2014) 1–8, https://doi.org/10.1186/1556-276X-9-290.

[58] C. Liu, T. Zhang, L. Cao, K. Luo, High-Capacity Anode Material for Lithium-Ion Batteries with a Core-Shell NiFe$_2$O$_4$/Reduced Graphene Oxide Heterostructure, ACS Omega 6 (2021) 25269–25276, https://doi.org/10.1021/acsomega.1c03050.

[59] H. Sun, G. Xin, T. Hu, M. Yu, D. Shao, X. Sun, J. Lian, High-rate lithiation-induced reactivation of mesoporous hollow spheres for long-lived lithium-ion batteries, Nat. Commun. 5 (2014), https://doi.org/10.1038/ncomms5526.

[60] X. Gao, J. Wang, D. Zhang, K. Nie, Y. Ma, J. Zhong, X. Sun, Hollow NiFe$_2$O$_4$ nanospheres on carbon nanorods as a highly efficient anode material for lithium ion batteries, J Mater Chem A Mater 5 (2017) 5007–5012, https://doi.org/10.1039/c6ta11058d.

[61] W. Xie, P. Guo, X. Gao, Elucidating the rate limitation of lithium-ion batteries under different charging conditions through polarization analysis, J Energy Storage 82 (2024), https://doi.org/10.1016/j.est.2024.110554.

[62] X. Tang, G. Sui, Q. Cai, W. Zhong, X. Yang, Novel MnO/carbon composite anode material with multi-modal pore structure for high performance lithium-ion batteries, J Mater Chem A Mater 4 (2016) 2082–2088, https://doi.org/10.1039/c5ta10073a.

[63] Y. Yang, Y. Zhao, L. Xiao, L. Zhang, Nanocrystalline ZnMn$_2$O$_4$ as a novel lithium-storage material, Electrochem. Commun. 10 (2008) 1117–1120, https://doi.org/10.1016/j.elecom.2008.05.026.

[64] S.-W. Kim, H.-W. Lee, P. Muralidharan, D.-H. Seo, W.-S. Yoon, D.K. Kim, K. Kang, Electrochemical performance and ex situ analysis of ZnMn$_2$O$_4$ nanowires as anode materials for lithium rechargeable batteries, Nano Res. 4 (2011) 505–510, https://doi.org/10.1007/s12274-011-0106-0.

[65] F.M. Courtel, Y. Abu-Lebdeh, I.J. Davidson, ZnMn$_2$O$_4$ nanoparticles synthesized by a hydrothermal method as an anode material for Li-ion batteries, Electrochim. Acta 71 (2012) 123–127, https://doi.org/10.1016/j.electacta.2012.03.108.

[66] J.G. Kim, S.H. Lee, Y. Kim, W.B. Kim, Fabrication of Free-standing ZnMn$_2$O$_4$ Mesoscale Tubular Arrays for Lithium-Ion Anodes with Highly Reversible Lithium Storage Properties, ACS Appl. Mater. Interfaces 5 (2013) 11321–11328, https://doi.org/10.1021/am403546s.

[67] X. Zeng, L. Shi, L. Li, J. Yang, X. Cheng, M. Gao, The preparation of flowerlike ZnMn$_2$O$_4$ microspheres assembled with porous nanosheets and their lithium battery performance as anode materials, RSC Adv. 5 (2015) 70379–70386, https://doi.org/10.1039/C5RA11473J.

[68] S. Gu, J. Xu, B. Lu, Crumpled ZnMn$_2$O$_4$ Nanosheets for Long-Term-Cycling Lithium-Ion Battery Anodes, Energ. Technol. 4 (2016) 1106–1111, https://doi.org/10.1002/ente.201600087.

[69] N. Ren, H. Jiu, L. Jiang, Q. Zhang, S. Yu, Y. Gao, Z. Gao, L. Zhang, Facile synthesis of hierarchical porous ZnMn$_2$O$_4$ rugby-balls on Ni foam for lithium-ion batteries with enhanced electrochemical properties, J. Alloys Compd. 740 (2018) 28–35, https://doi.org/10.1016/j.jallcom.2017.12.362.

[70] J. Zou, B. Liu, H. Liu, Y. Ding, T. Xin, Y. Wang, Facile synthesis of interconnected mesoporous ZnMn$_2$O$_4$ nano-peanuts for Li-storage via distinct structure design, Mater. Res. Bull. 107 (2018) 468–476, https://doi.org/10.1016/j.materresbull.2018.08.019.